Supporting Information for

Capillary-filling-regulated direct soft imprint lithography for coffee-ring- and residue-free stacked-layer patterning

Qi Zhou, Baozhong Chen, Jintao Xu, Huimin Su, Ruibin Liang, Yutian Liu, Kangxin Shen, Jiale Huang, Shuguang Zhang*, Linfeng Lan*, and Junbiao Peng

Q. Zhou, B. Chen, J. Xu, H. Su, R. Liang, Y. Liu, K. Shen, J. Huang, J. Peng

State Key Laboratory of Luminescent Materials and Devices, South China University of Technology, Wushan Road 381, Guangzhou 510640, P. R. China

Corresponding Author

Linfeng Lan - *Guangdong Basic Research Center of Excellence for Energy & Information Polymer Materials, State Key Laboratory of Luminescent Materials and Devices, South China University of Technology, Wushan Road 381, Guangzhou 510640, P. R. China;* E-mail: lanlinfeng@scut.edu.cn

Shuguang Zhang- *State Key Laboratory of Luminescent Materials and Devices, South China University of Technology, Wushan Road 381, Guangzhou 510640, P. R. China;* E-mail: mssgzhang@scut.edu.cn

Table S1. Viscosity, surface tension, and boiling points of the solvents

Solvent	Viscosity (cP)[a]	Surface tension (mN m^{-1})[a]	Boiling point (°C)[a]
2-ME	1.72	31.8	124.6
EG	21.00	48.4	197.3
ethanol	1.20	22.3	78.2
acetylacetone	1.95	30.2	140.4
N-methylpyrrolidone	1.65	40.7	202.0

a) All properties were taken from standard databases at 20 °C; boiling points at 1 atm.

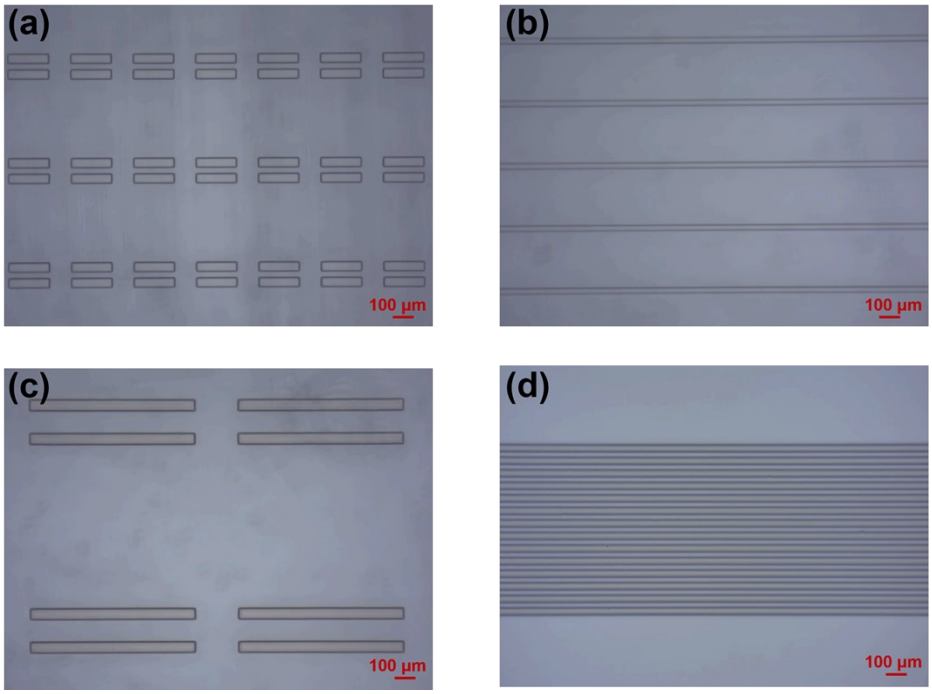

Fig. S1. POM images of the master mold.

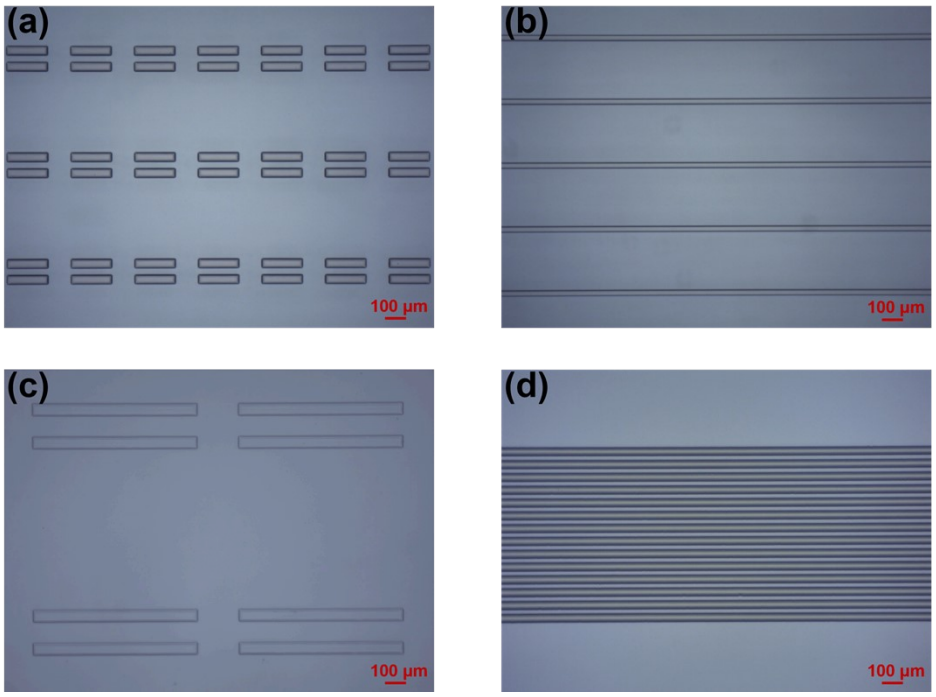

Fig. S2. POM images of the PDMS stamp.

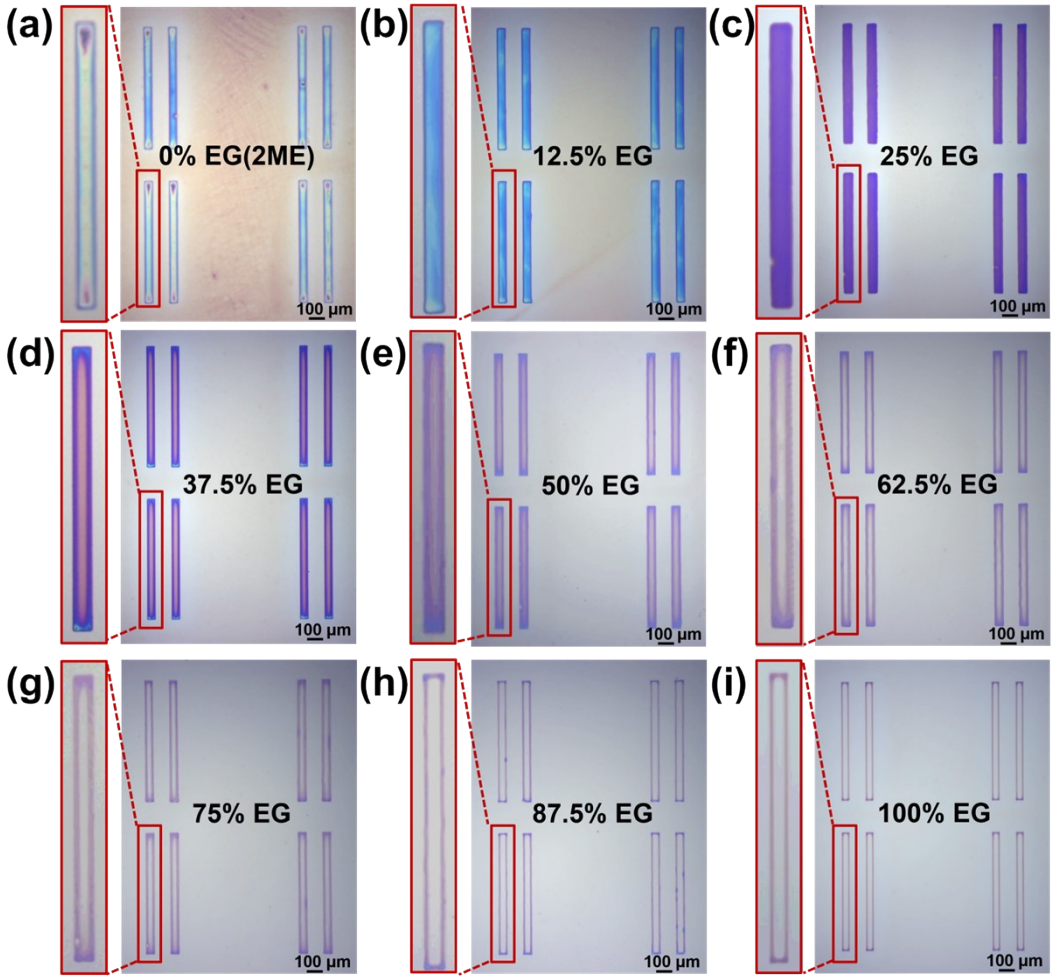

Fig. S3. (a-i) POM images of ITO patterns imprinted on SiO_2/Si substrates using plasma-treated PDMS stamps and ITO inks with EG fraction from 0 to 100 vol% (in 12.5 vol% increments). Scale bar: 100 μm.

Table S2. Contact angles of ITO inks with EG containing 0, 25, 50, and 100 vol% on treated/untreated PDMS (25 °C)

EG content (%)	0	25	50	100
untreated θ (°)	62.2-68.5	69.8-74.5	68.7-76.1	86.3-89.4
treated θ (°)	<5	<5	<5	<5

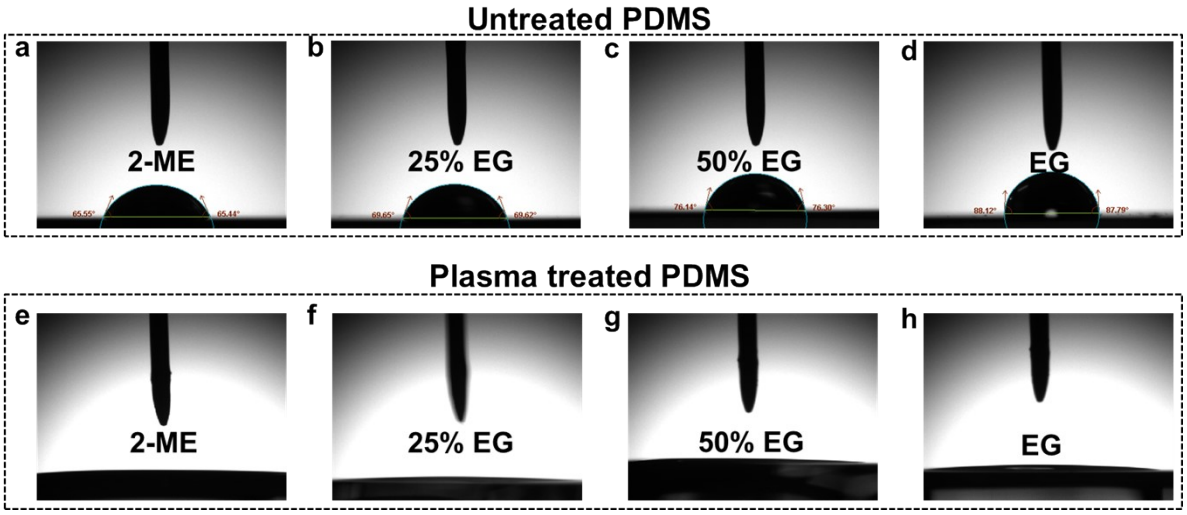

Fig. S4. The optical images of the contact angle measurement for ITO inks on untreated/treated PDMS with EG fraction of 0, 25, 50, and 100 vol%.

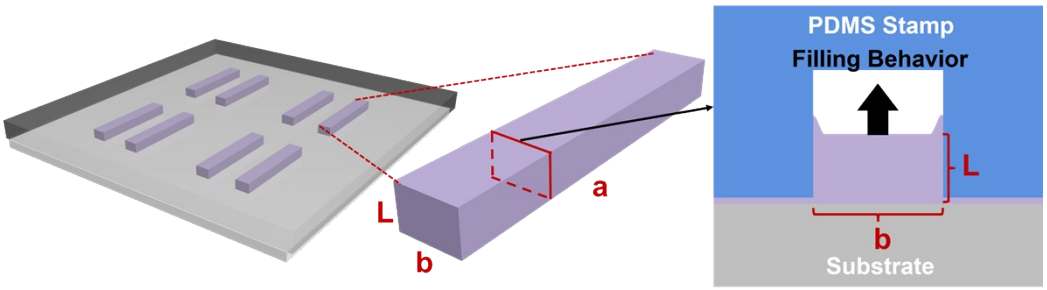

Fig. S5. The illustration of the ink filling into the PDMS microchannels and geometric dimensions.

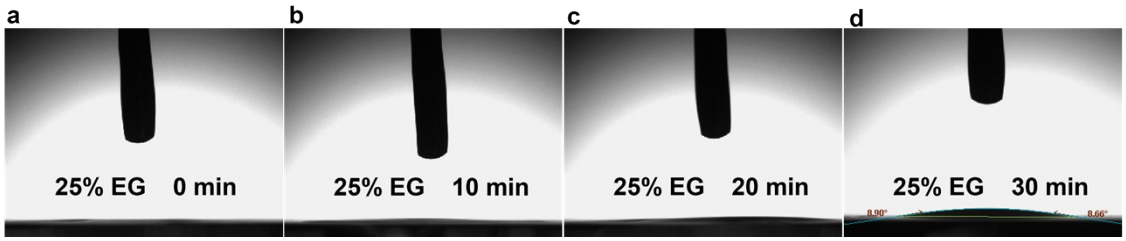

Fig. S6. The hydrophobic recovery of plasma-treated PDMS.

Table S3. Summary of the related data of the fitting of H_n^2/γ as a function of viscosity at 70 ℃ for ITO inks containing 0-100 vol% EG (in 12.5% increments)

EG content (%)	0	12.5	25.0	37.5	50.0	62.5	75.0	87.5	100.0
η (cP, fitting at 70 ℃)	0.52	0.83	1.08	1.37	1.82	2.22	2.64	3.21	3.93
S (nm)	115	69	48	40	26	21	18	15	12
H_n^2 (μm^2)	80.609	29.019	14.043	9.752	4.12	2.688	1.975	1.371	0.878
γ (mN m^{-1})	27.3	29.29	30.79	33.71	35.33	37.89	40.18	44.94	48.06
H_n^2/γ (mm^3 N^{-1})	2.953	0.991	0.456	0.289	0.117	0.0709	0.0492	0.0305	0.0183

To facilitate curve fitting, the units were not uniformly converted to SI units. In order to acquire the fitted curves in the International System of Units, we implemented the following corrections to the fitting parameters through dimensional analysis:

$A_{2,\,SI}=A_2\times10^{-3(C+1)-9}$

$B_{2,\,SI}=B_2\times10^{3C}$

$C_{2,\,SI}=C_2$

$D_{2,\,SI}=D_2\times10^{-9}$

Calculated results:

$A_{2,\,SI}$ = 7.5202×10^{-21} (Pa s)$^{C+1}$ m^2 s^2 kg^{-1}

$B_{2,\,SI}$ = 6.6534×10^8 (Pa s)$^{C+1}$

$C_{2,\,SI}$ = 2.4353 (No dimension)

$D_{2,\,SI}$ = 2.15×10^{-11} m^3 N^{-1}

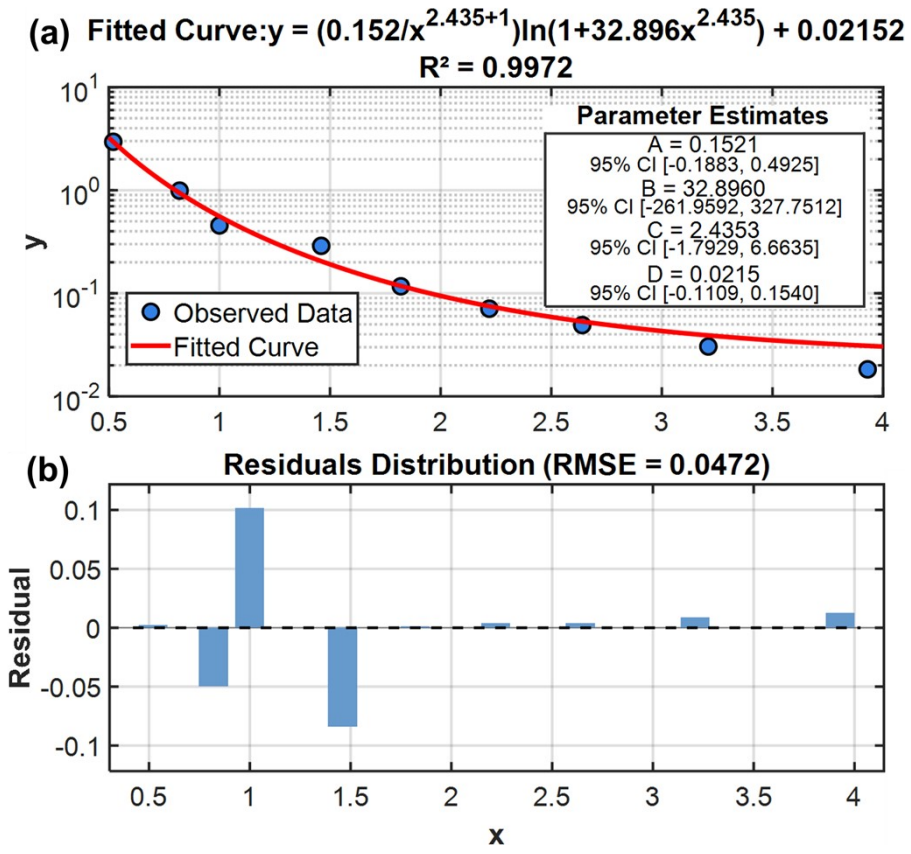

Fig. S7. (a) The fitted curve of H_n^2/γ as a function of viscosity at 70℃ of inks and (b) the residual distribution plot of the fitted results.

Table S4. The measured ITO thickness and predicted ITO thickness using untreated PDMS with ITO inks containing 0, 25, and 50 vol% EG.

EG percentage (%)	0	25	50
measured S (nm)	75	28	17
θ of PDMS (°)	62.2–68.5	69.8–74.5	68.7–76.1
estimated S (nm)	70–79	26–29	14–17

Table S5. Comparison of representative patterning approaches used in printed electronics

Method	**Feature Size (μm)**	**Cost**	**Fidelity**	**Coffee Ring**	**Residue**	**Ref.[d]**
Spray Coating	50-100	Low	Low	Present	N/A[c]	[1]
Screen Printing	30-100	Low	Low	Present	N/A[c]	[2]
Inkjet	20-50	Low	Low	Present	N/A[c]	[3,4]
NIL	<1	High	Very High	N/A[c]	Present	[5]
Gravure Printing	20-50	Moderate	Moderate	Present	Present	[6-8]
Standard solution-based DSIL	0.1-100	Low	Low to High[b]	Present	Present	[9-14]
IPA-assisted DSIL of Ag Inks (monolayer)[a]	20	Low	High	Suppressed	Suppressed	[15]
This Work (metal-oxide precursors, stacked-layer)	10	Low	High	Suppressed	Suppressed	N/Ac

(a) IPA-assisted DSIL of Ag Inks, our previous work.

(b) Low to High, depending on processing conditions.

(c) N/A = not applicable.

(d) References in this table correspond to those listed in the Supporting Information.

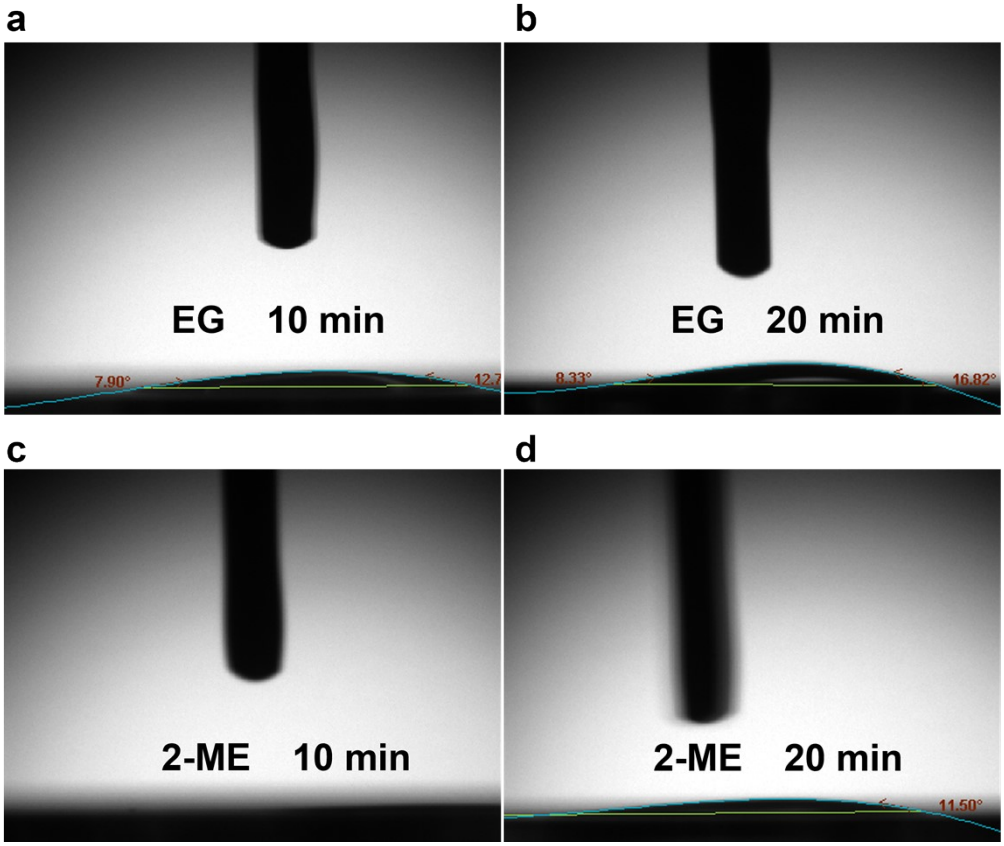

Fig. S8. Advancing and receding contact angles of the EG-based and 2-ME-based ITO precursor inks on plasma-treated PDMS at 10 and 20 min after plasma activation, measured using the tilting-plate method.

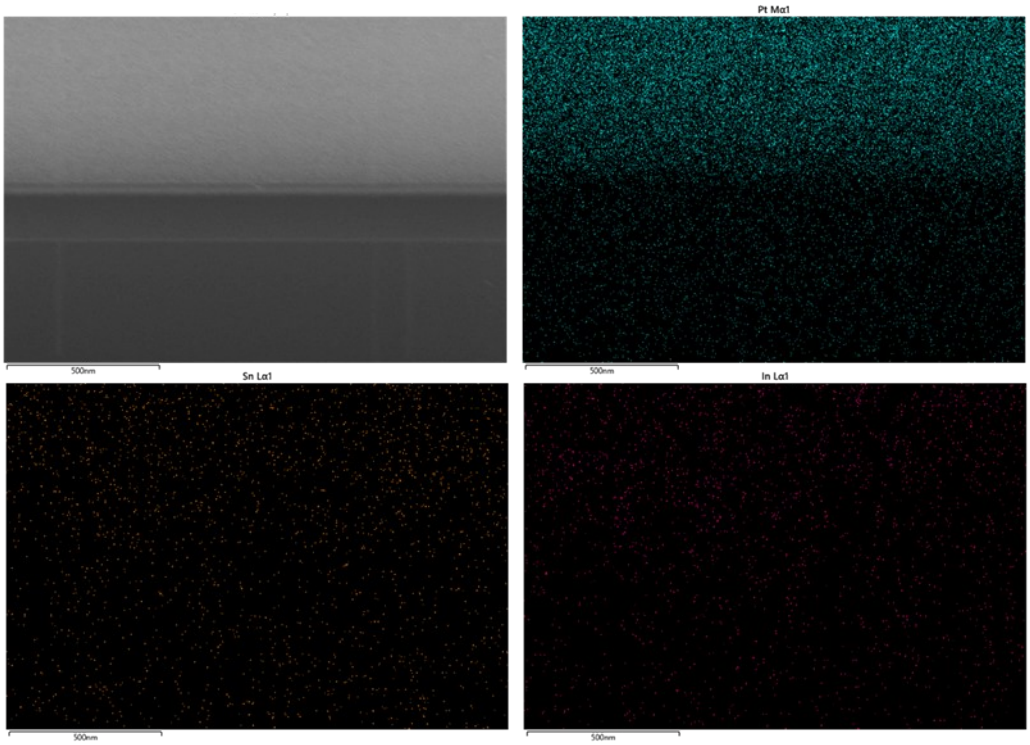

Fig. S9. Cross-sectional SEM image and corresponding EDS elemental maps (In, Sn) of the region between two ITO electrodes after imprinting.

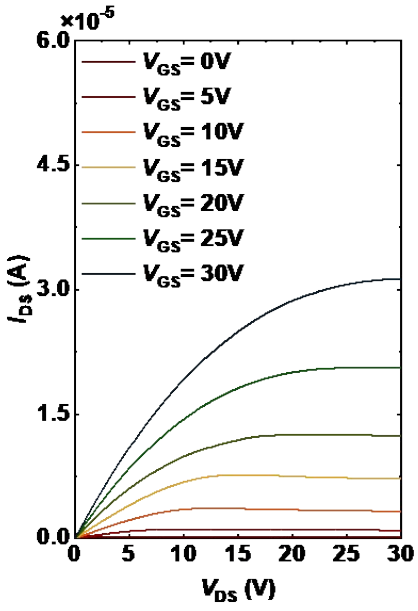

Fig. S10. Representative output characteristics of the bottom-contact TFTs measured at different gate voltages.

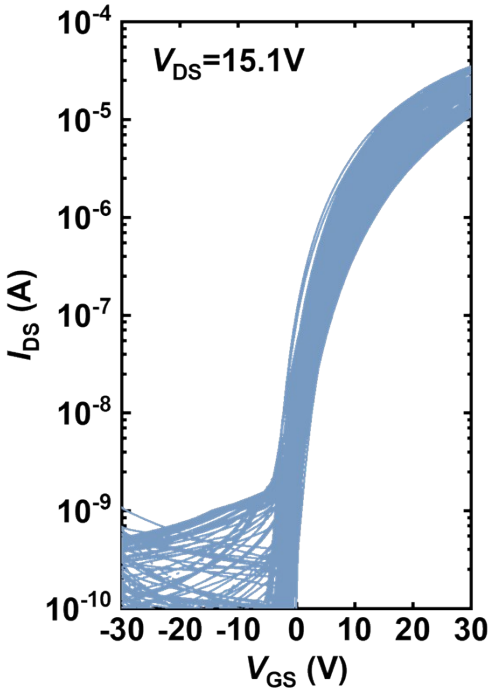

Fig. S11. Transfer characteristics of 50 bottom-contact TFTs.

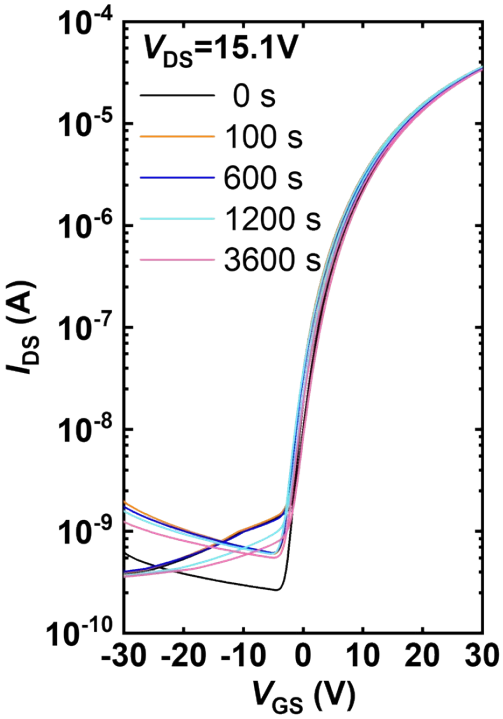

Fig. S12. PBS experiment for the bottom-contact TFT at the gate voltage of 20 V for 3600 s.

Hydrodynamic model based on capillary filling dynamics for DSIL

According to the Hagen-Poiseuille law[16,17], the volumetric flow rate of fluids in the rectangular channel can be expressed as

$$Q = ab^3 f(a/b)/12\eta L\Delta P \qquad f(a/b) = 1 - \sum_{n=2k-1}^{\infty} \frac{192btanh(n\pi a/2b)}{\pi^5 a \qquad n^5}(k = 1,2,3\ldots) \tag{S1}$$

where a and b represent the length and width of the rectangular channel, respectively; L is the filling distance of the rectangular channel; η is the dynamic viscosity; ΔP is the pressure difference; and $f(a/b)$ is geometric correction for Poiseuille flow in rectangles.

According to the relationship between the volumetric flow rate and mean flow velocity, Q can alternatively be expressed as

$$Q = abL/t \tag{S2}$$

where t is the time for fluid flow within the channel. Considering only viscous resistance, the pressure drop ΔP_1 required to fill a rectangular tube over a distance L in time t can be derived from Eq. (S1) and Eq. (S2) as

$$\Delta P_1 = 12\eta L^2/tb^2 f(a/b) \tag{S3}$$

In addition to viscous resistance, as discussed earlier, capillary pressure also influences fluid flow. According to the Laplace pressure equation, the capillary pressure can be expressed as

$$\Delta P_2 = 2\gamma(1/a + 1/b)cos\theta \tag{S4}$$

This capillary pressure acts as a driving pressure on the fluid. Therefore, the net pressure difference required to drive the fluid flow during the imprinting process can be expressed as

$$\Delta P = 12\eta L^2/tb^2 f(a/b) - 2\gamma(1/a + 1/b)cos\theta \tag{S5}$$

Based on Eq. (S5), the filling capacity of the ink into the PDMS microchannels during imprinting is governed by the ink viscosity, contact angle, and microchannel dimensions. For a given PDMS stamp, only the ink viscosity and contact angle require optimization, which reinforces our previous analysis. The first term in Eq. (S5) represents viscous resistance, while the second term quantifies capillary pressure.

For quantitative analysis, the rectangular-channel-adapted Lucas-Washburn equation[18] can be derived by equating ΔP_1 and ΔP_2 after coupling Eq. (S1) and the differential form of Eq. (S2):

$$L = \sqrt{\frac{m\gamma cos\theta}{3\eta}}\sqrt{t}, \quad m = b/a(a + b)f(a/b) \tag{S6}$$

where L is the filling distance of the fluid, and m is a dimensional shape factor. Under steady laminar flow conditions, substituting the measured parameters (a = 800 μm, b = 60 μm, cos $\theta \approx 1$, $\eta_{25\ vol\%\ EG}$ = 4.87 cp, and γ = 27.37 mN/m) into Eq. (S6) yields a maximum filling distance L_{max} = 2 μm (microchannel length) at $t = 7\times10^{-8}$ s.

It reveals that the filling process completes instantly. Further calculations using an ink density $\rho \approx 1$ g/cm³ and characteristic dimension d = 100 μm yield the Reynolds number (Re) ≈ 0.003 (substantially below 1), thereby confirming the assumption of steady laminar flow. These results indicate that DSIL may entail a two-stage mechanism: the complete filling of microchannels with low-concentration ink, followed by concurrent evaporation and refilling. Therefore, Eq. (S6) only describes the initial filling dynamics during the imprinting process.

To analyze the entire filling process, a power-law modification accounting for viscosity changes due to solvent evaporation was introduced:

$$\eta_e(t) = K_1\eta(1 + \alpha\eta^c t) \tag{S7}$$

Combined Eq. (S7) and the initial conditions, the total filling height H can be rewritten as

$$H = \sqrt{\frac{m\gamma cos\theta}{3K_1\alpha\eta^{C+1}} ln(1 + \alpha\eta^c t) + (K_2H_0)^2}, \quad m = b/a(a+b)f(a/b)\ (H_0 = 2\ \mu m, \theta < 90°) \tag{S8}$$

where K_1 ($K_1 > 1$) is the spin-coating technological coefficient; α characterizes evaporation in the imprinting process; C is power-law index; and K_2 ($K_2 < 1$) is the modification coefficient accounting for ink loss. The increase in η after spin-coating reduces the Re, thus maintaining steady laminar flow. As contact angle (θ) approaches 90° (and cos θ approaches 0), the total filling height H approaches zero. Consequently, the ink fails to fill the PDMS microchannels, which accounts for the failure of the ITO film formation in Fig. 2b (100 vol% EG).

Temperature is another parameter that requires to be considered. The DSIL process was conducted at 70°C (343.15K), whereas the initial viscosity properties were measured at room temperature. The η can be estimated using the Arrhenius viscosity equation:

$$\eta = A_0\, exp(E_a/RT) \tag{S9}$$

where A_0 is the pre-exponential factor; E_a is the viscosity activation energy; R is the gas constant; and T is the absolute temperature. The viscosity activation energy of the binary system follows an empirical formula:

$$E_a(\varphi) = E_{a_{EG}}\varphi + E_{a_{2-ME}}(1-\varphi) + g\varphi(1-\varphi) \tag{S10}$$

where φ is the percentage of EG, and g is the excess interaction parameter[19]. Using the lsqcurvefit function (MATLAB Optimization Toolbox, R2024b) for nonlinear least-squares fitting, the fitting curve of η versus φ is defined as

$$y = G\, exp(Ex + Fx^2),\ G = \eta_{2-ME},\ E = (E_{a_{EG}} - E_{a_{2-ME}} + g)/RT,\ F = -g/RT \tag{S11}$$

where y is η and x is φ. Fig. S13 shows excellent nonlinear fitting agreement with experimental data ($R^2 > 0.99$, RMSE = 0.3901). The parameter g was determined as 2307 J/mol. Combining this with the activation energy E_a

of EG (33700 J/mol) with Eq. (S9), η can be estimated at 70 °C for any φ (see Table S6)[20].

Table S6. Viscosity at 25 °C and 70 °C, and viscosity activation energy versus EG volume fraction (0-100 vol% in 12.5% steps)

EG content (%)	0	12.5	25.0	37.5	50.0	62.5	75.0	87.5	100.0
η (cP, measurement at 25 °C)	2.28	3.81	4.87	7.37	9.56	12.10	14.90	18.60	23.40
E_a (J mol^{-1})	27970	28939	29811	30638	31412	32092	32700	33236	33700
η (cP, fitting at 70 °C)	0.52	0.83	1.08	1.37	1.82	2.22	2.64	3.21	3.93

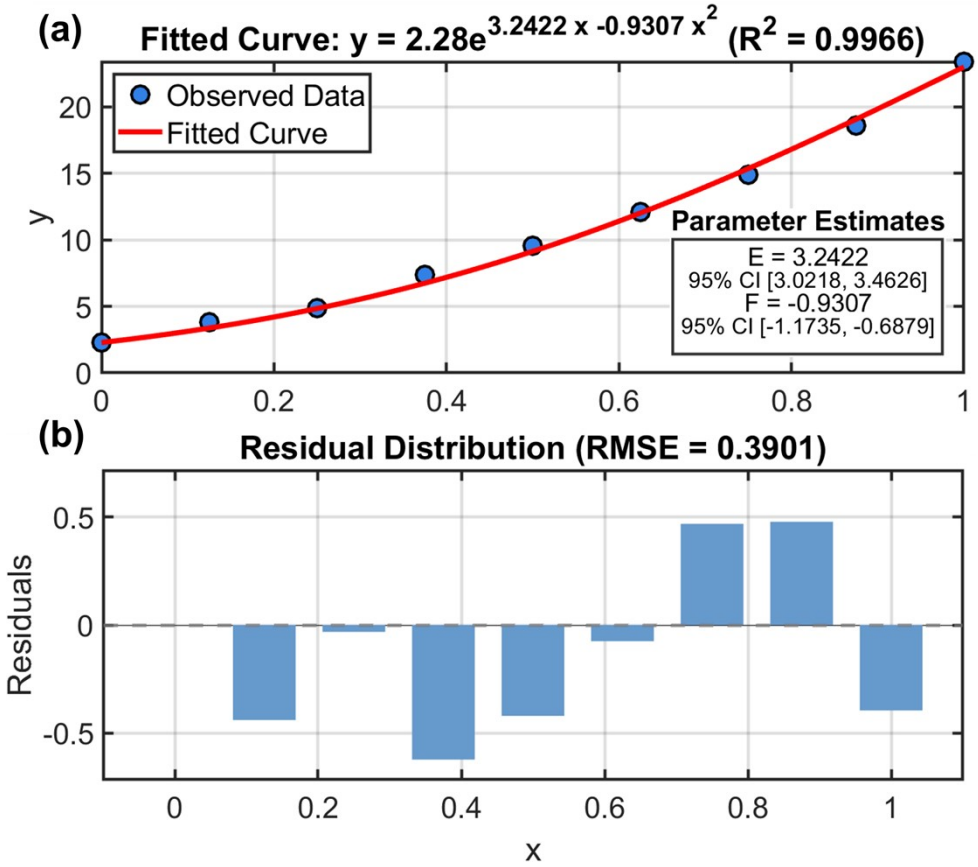

Fig. S13. (a) The fitted curve of the ink viscosity as a function of EG ratios and (b) the residual distribution plot of the fitted results.

The specific numerical value H_n of the total filling height is determined by conservation of the amount of substance:

$$H_n = 2K_3S\rho/cM \ (H_n = K_3H) \tag{S12}$$

where K_3 ($K_3 < 1$) is the concentration correction coefficient; c is the molar concentration of the ITO inks; M (278 g/mol) is the molar mass of $In_{1.9}Sn_{0.1}O_3$, and ρ (5.426g/cm^3) is the density of the ITO films measured by X-ray

reflectometry (XRR) (Fig. S14). The term *S* represents the area-averaged thickness obtained by integrating the thickness profile in Fig. 2c (plasma-treated PDMS).

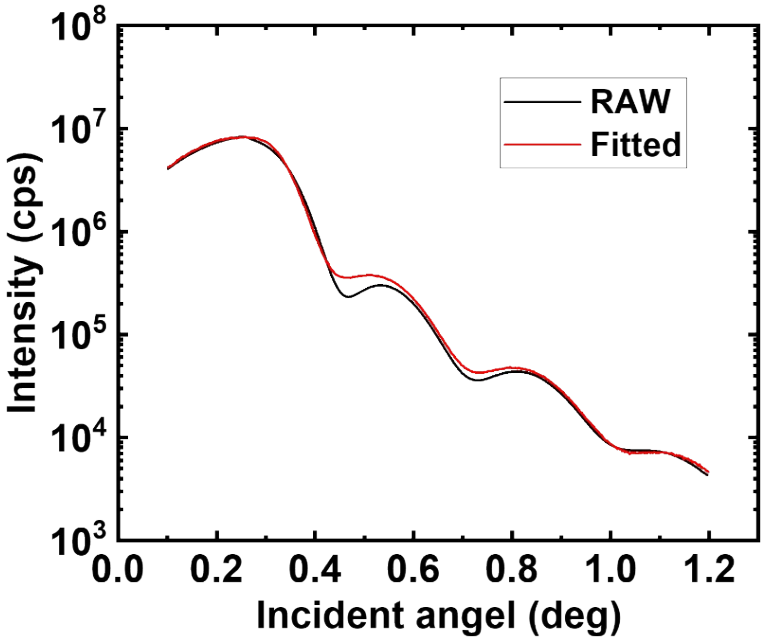

Fig. S14. XRR spectra of the ITO film.

To evaluate the validity of the physical model described by Eq. (S8), we employ nonlinear least-squares fitting using the following function of:

$$y = \frac{A}{x^{C+1}} ln(1 + Bx^{C}) + D \quad A = \frac{mK_3^2 cos\theta}{3K_1\alpha}, \quad B = \alpha t, \quad C = c, \quad D = \frac{(K_2K_3H_0)^2}{\Upsilon}, \quad m = b/a(a+b)f(a/b) \tag{S13}$$

where y is H_n^2/γ, x is η and C is a dimensionless parameter. The dimensions of A, B and D are $(Pa{\cdot}s)^{C+1}{\cdot}m^2s^2/kg$, $(Pa{\cdot}s)^{C+1}$ and m^3/N, ensuring that the product $B\eta^C$ remains dimensionless. Fig. S7 shows the results of the nonlinear fitting ($\cos\theta$ is approximated as 1), demonstrating good agreement with experimental data ($R^2 > 0.99$, RMSE = 0.0472). To further validate the physical model of Eq. (S13), the thickness in Fig. 2c (untreated PDMS) was estimated based on the fitting results. The estimated value agrees well with the measured value. Using the fitted parameters A, B (calibrated in SI units) and K_3 ($0.1 < K_3 < 1$), the order of magnitude of η at the final imprinting stage (t = 14 min) was estimated to be 10^5~10^9 Pa·s, an exceptionally high value. At such magnitudes, continued filling requires substantial additional imprinting pressure to overcome viscous resistance [21]. Consequently, the filling velocity of the inks gradually decreases during the imprinting process, eventually stopping before the process was terminated.

For Eq. (S13), the fit has four free parameters (A, B, C, D), while γ, θ, η, a, and b are measured and fixed. The relatively wide 95% CIs of A, B, C, and D should be attributed to parameter collinearity rather than model inadequacy. This collinearity preserves the fitted curve shape by allowing changes in other parameters to offset a change in one parameter, which accounts for the relatively wide 95% CIs. The curve is governed by the composite $A\ ln(1 + Bx^C)/x^{C+1}$, so various sets of parameters yield essentially the same fitted shape. Since our objective is to validate the form of Eq. (S13) rather than determine the precise value of each parameter, we interpret A, B, C, and D as effective composite parameters. The shape validity is supported by the excellent fits ($R^2 \approx 1$) and predictions on untreated PDMS, confirming that the proposed hydrodynamic model remains valid for different inks, microchannel geometries, and surface conditions.

References

1 K. Lee, J. G. Oh, D. Kim, J. Baek, I. H. Kim, S. Nam, Y. J. Jeong, J. Jang, *Appl. Surf. Sci.*, 2023, **608**, 155081.

2 L. Liu, Z. Shen, X. Zhang, H. Ma, *J. Colloid Interface Sci.*, 2020, **582**, 12-21.

3 M. Caironi, E. Gili, T. Sakanoue, X. Cheng, H. Sirringhaus, *ACS Nano*, 2010, **4**, 1451-1456.

4 Y. Li, L. Lan, P. Xiao, S. Sun, Z. Lin, W. Song, E. Song, P. Gao, W. Wu, J. Peng, *ACS Appl. Mater. Interfaces*, 2016, **8**, 19643-19648.

5 X. Zhang, N. Sui, M. Li, S. Wang, S. Shao, W. Liu, J. Sun, J. Yang, J. Zhao, *Nano Res.*, 2025, **18**, 94907350.

6 J. Zhang, X. Hu, J. Zhang, Y. Cui, C. Yuan, H. Ge, Y. Chen, W. Wu, Q. Xia, *Nanoscale Res Lett.*, 2012, **7**, 380.

7 P. Choi, P. F. Fu, L. Guo, Siloxane Copolymers for Nanoimprint Lithography, *Adv. Funct. Mater.*, 2007, **17**, 65-70.

8 M. Leitgeb, D. Nees, S. Ruttloff, U. Palfinger, J. Götz, R. Liska, M. R. Belegratis, B. Stadlober, *ACS Nano*, 2016, **10**, 4926-4941.

9 O. F. Göbel, D. H. A. Blank, J. E. T. Elshof, *ACS Appl. Mater. Interfaces*, 2010, **2**, 536-543.

10 S. Seraji, Y. Wu, N. E. Jewell-Larson, M. J. Forbess, S. J. Limmer, T. P. Chou, G. Cao, Patterned Microstructure of Sol-Gel Derived Complex Oxides Using Soft Lithography, *Adv. Mater.*, 2000, **12**, 1421-1424.

11 I. Park, J. Cheng, A. P. Pisano, E. Lee, J. H. Jeong, *Appl. Phys. Lett.*, 2007, **90**, 093902.

12 S. H. Ko, I. Park, H. Pan, C. P. Grigoropoulos, A. P. Pisano, C. K. Luscombe, J. M. J. Fréchet, *Nano Lett.*, 2007, **7**, 1869-1877.

13 X. Luo, M. Yang, J. Bu, T. Chen, A. Y. Yi, W. Xu, *Macromol. Res*, 2023, **31**, 795-803.

14 R. Kothari, M. R. Beaulieu, N. R. Hendricks, S. Li, J. J. Watkins, *Chem. Mater*, 2017, **29**, 3908-3918.

15 Q. Zhou, L. Lan, Y. Li, B. Chen, B. Huang, H. Su, J. Xu, S. Yang, J. Peng, *ACS Appl. Mater. Interfaces*, 2024, **16**, 27560-27565.

16 B. J. Bayly, S. A. Orszag, T. Herbert, *Annu. Rev. Fluid Mech.*, 1988, **20**, 359-391.

17 L.M. Milne-Thomson, Theoretical Hydrodynamics, Macmillan, London, 1968, p. 672.

18 R. Lucas, *Colloid Polym. Sci.*, 1918, **23**, 15-22.

19 J. Kunnen, *Rheologica Acta.*, 1984, **23**, 424-434.

20 V. V. Loskutov, *J. Solution Chem.*, 2021, **50**, 427-442.

21 J. Thomas, P. Gangopadhyay, E. Araci, R. A. Norwood, N. Peyghambarian, *Adv. Mater.*, 2011, **23**, 4782-4787.